

1 **Tropopause Evolution in a Rapidly Intensifying Tropical Cyclone: A Static**
2 **Stability Budget Analysis**

3 Patrick Duran* and John Molinari

4 *University at Albany, State University of New York, Albany, NY*

5 **Corresponding author address:* Department of Atmospheric and Environmental Sciences, Univer-
6 sity at Albany, State University of New York, 1400 Washington Avenue, Albany, NY.

7 E-mail: pduran2008@gmail.com

ABSTRACT

⁸ We have some cool results!

9 **1. Introduction**

10 Perhaps introduce upper-tropospheric static stability and its relationship to the diurnal cycle
11 before going into Patricia? Include references to Dunion, Navarro, and O'Neill here.

12 More recently, Dunion et al. (2014) documented a periodic oscillation of infrared brightness
13 temperature in hurricanes, which they call the "TC diurnal pulse." There will be a whole bunch of
14 papers cited here...

15 After undergoing a remarkably rapid intensification (RI), Hurricane Patricia (2015) set a new
16 record as the strongest tropical cyclone (TC) ever observed in the Western Hemisphere (Kim-
17 berlain et al. 2016; Rogers et al. 2017). High-altitude dropsonde observations taken during
18 the Tropical Cyclone Intensity (TCI) Experiment captured this RI in unprecedented detail (Doyle
19 et al. 2017). These observations revealed remarkable changes in the structure of the cold-point
20 tropopause and upper-level static stability as the storm intensified (Duran and Molinari 2018). At
21 tropical storm intensity, shortly before RI commenced, a strong inversion layer existed just above
22 Patricia's cold-point tropopause, which was located near 17.2 km. During the first half of the RI
23 period, this inversion layer weakened throughout Patricia's inner core, with the weakening most
24 pronounced over the developing eye. By the time the storm reached its maximum intensity, the
25 inversion layer over the eye had disappeared almost completely, which was accompanied by an
26 increase in the tropopause height to a level at or above the highest-available dropsonde data point
27 (18.3 km) at two locations. Meanwhile over the eyewall region, the static stability re-strengthened
28 and the tropopause was limited to a level at or below 17.5 km. The mechanisms that led to these
29 changes in upper-level static stability and tropopause height are the subject of the current paper.

30 INCLUDE IN THIS INTRODUCTION DAN STERN'S POTENTIAL TEMPERATURE BUD-
31 GET PAPERS

32 At some point (probably in the Discussion) mention the possible importance of static stability
33 asymmetries, in the context of the Diurnal pulse

34 **2. Model Setup**

35 The numerical simulations were performed using version 19.4 of Cloud Model 1 (CM1) de-
36 scribed in Bryan and Rotunno (2009). The equations of motion were integrated on a 3000-km-
37 wide, 30-km-deep axisymmetric grid with 1-km horizontal and 250-m vertical grid spacing. The
38 computations were performed on an f -plane at 15°N latitude, over a sea surface with constant
39 temperature of 30.5°C, which matches that observed near Hurricane Patricia (2015; Kimberlain
40 et al. 2016). Horizontal turbulence was parameterized using the Smagorinsky scheme described in
41 Bryan and Rotunno (2009, pg. 1773), with a prescribed mixing length that varied linearly from 100
42 m at a surface pressure of 1015 hPa to 1000 m at a surface pressure of 900 hPa. This formulation
43 allows for realistically-large horizontal mixing lengths near the hurricane’s inner core, consistent
44 with the results of Bryan (2012), while not over-representing horizontal turbulence in convection
45 at outer radii. Vertical turbulence was parameterized using the formulation of Markowski and
46 Bryan (2016, their Eq. 6), using an asymptotic vertical mixing length of 100 m. A Rayleigh
47 damping layer was applied outside of the 2900-km radius and above the 25-km level to prevent
48 spurious gravity wave reflection at the model boundaries. Microphysical processes were param-
49 eterized using the Thompson et al. (2004) microphysics scheme and radiative heating tendencies
50 were computed every two minutes using the Rapid Radiative Transfer Model for GCMs (RRTMG)
51 longwave and shortwave schemes (Iacono et al. 2008). The initial temperature and humidity field
52 was horizontally-homogeneous and determined by averaging all Climate Forecast System Reanal-
53 ysis (CFSR) grid points within 1000 km of Patricia’s center of circulation at 18 UTC 21 October

2015. The vortex described in Rotunno and Emanuel (1987, their Eq. 37) was used to initialize the wind field, setting all parameters equal to the values used therein.

Although hurricanes simulated in an axisymmetric framework tend to be more intense than those observed in nature, the intensity evolution of this simulation matches reasonably well with that observed in Hurricane Patricia. After an initial spin-up period of about 20 hours, the modeled storm (Fig.1, blue lines) began an RI period that lasted approximately 30 hours. After this RI, the storm continued to intensify more slowly until the maximum 10-m wind speed reached 89 m s^{-1} and the minimum sea-level pressure reached its minimum of 846 mb, 81 hours into the simulation. Hurricane Patricia (red stars) exhibited a similar intensity evolution, with an RI period leading to a maximum 10-m wind speed of 95 m s^{-1} and a minimum sea-level pressure of 872 hPa. Despite the limitations of the axisymmetric framework, the extraordinary intensity of Hurricane Patricia and the rapidity of its intensification makes Patricia a particularly good candidate for axisymmetric analysis.

3. Budget Computation

The static stability can be expressed as the squared Brunt Väisälä frequency:

$$N_m^2 = \frac{g}{T} \left(\frac{\partial T}{\partial z} + \Gamma_m \right) \left(1 + \frac{T}{R_d/R_v + q_s} \frac{\partial q_s}{\partial T} \right) - \frac{g}{1 + q_t} \frac{\partial q_t}{\partial z}, \quad (1)$$

where g is gravitational acceleration, T is temperature, R_d and R_v are the gas constants of dry air and water vapor, respectively, q_s is the saturation mixing ratio, q_t is the total condensate mixing ratio, and Γ_m is the moist-adiabatic lapse rate:

$$\Gamma_m = g(1 + q_t) \left(\frac{1 + L_v q_s / R_d T}{c_{pm} + L_v \partial q_s / \partial T} \right), \quad (2)$$

where L_v is the latent heat of vaporization and c_{pm} is the specific heat of moist air at constant pressure. In the tropopause layer, q_s , $\partial q_s / \partial T$, and $\partial q_t / \partial z$ approach zero. In this limiting case,

Eq. 1 reduces to:

$$N^2 = \frac{g}{\theta_v} \frac{\partial \theta_v}{\partial z}, \quad (3)$$

where θ_v is the virtual potential temperature. To compute N^2 , CM1 uses Eq.1 in saturated environments and Eq. 3 in sub-saturated environments. For simplicity, however, only Eq. 3 will be used for the budget computations herein¹.

Taking the time derivative of Eq. 3 yields the static stability tendency:

$$\frac{\partial N^2}{\partial t} = \frac{g}{\theta} \frac{\partial}{\partial z} \frac{\partial \theta}{\partial t} - \frac{g}{\theta^2} \frac{\partial \theta}{\partial z} \frac{\partial \theta}{\partial t}, \quad (4)$$

where the potential temperature tendency, $\partial \theta / \partial t$, can be written:

$$\frac{\partial \theta}{\partial t} = HADV + VADV + HTURB + VTURB + MP + RAD + DISS \quad (5)$$

Each term on the right-hand side of Eq.5 represents a potential temperature budget variable, each of which is output directly by the model every minute. HADV and VADV are the radial and vertical advective tendencies, HTURB and VTURB are the radial and vertical tendencies from the turbulence parameterization, MP is the tendency from the microphysics scheme, RAD is the tendency from the radiation scheme, and DISS is the tendency due to turbulent dissipation. This equation neglects Rayleigh damping, since this term is zero everywhere below 25 km, and the analysis domain does not extend to that level. Each term in Eq. 5 is substituted for $\partial \theta / \partial t$ in Eq. 4, yielding the contribution of each budget term to the static stability tendency. These terms are summed, yielding an instantaneous "budget change" in N^2 every minute. The budget changes are then averaged over 24-hour periods and compared to the total model change in N^2 over that same time period using a residual, i.e.:

$$\Delta N_{budget}^2 = \frac{1}{\delta t} \sum_{t=t_0}^{t_0+\delta t} \frac{\partial N^2}{\partial t} \Big|_t \quad (6)$$

¹The validity of this approximation will be substantiated later in this section.

$$\Delta N_{model}^2 = N_{t_0+\delta t}^2 - N_{t_0}^2 \quad (7)$$

$$Residual = \Delta N_{model}^2 - \Delta N_{budget}^2 \quad (8)$$

where t_0 is an initial time and δt is 24 hours.

Eqs. 6-8 are plotted for four consecutive 24-hour periods in Fig. 2. For this and all subsequent radial-vertical cross sections, a 1-2-1 smoother is applied once in the radial direction to eliminate $2\Delta r$ noise that appears in some of the raw model output and calculated fields. The left column of Fig. 2 depicts the model changes (Eq. 7), the center column depicts the budget changes (Eq. 6), and the right column depicts the residuals (Eq. 8). In every 24-hour period, the budget changes are nearly identical to the model changes, which is reflected in the near-zero residuals in the right column. This indicates that the budget accurately represents the model variability, which implies that the neglect of moisture in the budget computation introduces negligible error within the analysis domain².

In the tropopause layer, some of the budget terms are small enough to be ignored. To determine which of the budget terms are most important, a time series of the contribution of each of the budget terms in Eq. 5 to the tropopause-layer static stability tendency is plotted in Fig. 4. For this figure, each of the budget terms is computed using the method described in Section 3, except with 1-hour averaging intervals instead of 24-hour intervals. The absolute values of these tendencies are then averaged over a radius-height domain surrounding the tropopause and plotted as a time series³. Advection (Fig. 4, red line) plays an important role in the mean tropopause-layer

²This is not the case in the lower- and mid-troposphere, where the residual actually exceeds the budget variability in many places, likely due to the neglect of moisture; thus we limit this analysis to the upper troposphere and lower stratosphere.

³It will be seen in subsequent figures that each of the terms contributes both positively and negatively to the N^2 tendency within the analysis domain. Thus, taking an average over the domain tends to wash out the positive and negative contributions. To circumvent this problem, the absolute value of each of the terms is averaged, yielding a time series of the mean magnitude of each budget term.

static stability tendency at all times, and vertical turbulence (Fig. 4, blue line) and radiation (Fig. 4, dark green line) also contribute significantly. Although the contribution from horizontal turbulence (Fig. 4, purple line) becomes more important after 48 hours, it is confined to a very small region immediately surrounding the eyewall tangential velocity maximum (not shown), and is negligible throughout the rest of the tropopause layer. The remaining two processes - microphysics and dissipative heating (Fig. 4, orange and light green lines, respectively) - lie atop one another near zero. These time series indicate that, at all times, three budget terms dominate the tropopause-layer static stability tendency: advection, vertical turbulence, and radiation. Variations in the magnitude and spatial structure of these terms drive the static stability changes depicted in Fig. 2; subsequent sections will focus on these variations and what causes them.

4. Results

a. Static stability evolution

The average N^2 over the first day of the simulation (Fig. 3a) indicates the presence of a weak static stability maximum just above the cold-point tropopause. This lower-stratospheric stable layer had begun to erode during the initial spin-up period, with the maximum destabilization occurring at the innermost radii. This decrease in static stability continued into the second day of the simulation (Fig. 3b) as the storm intensified to hurricane strength (Fig. 1). Destabilization was particularly pronounced over the developing eye, where the time-mean cold-point tropopause height increased by up to one km compared to the previous day. Over the developing eyewall and rainband regions, meanwhile, the tropopause height remained nearly constant. During the third day of the simulation (Fig. 3c), static stability over the eye continued to decrease, and the cold-point tropopause height rose to nearly 20 km over the eye. The tropopause sloped sharply

132 downward outside of the 20-km radius, reaching a minimum altitude of 16.4 km only 45 km from
133 the storm center. This local minimum in tropopause height corresponded to the eyewall region,
134 where upper-tropospheric static stability increased during this time period. At larger radii, static
135 stability began to increase in the layer immediately overlying the cold-point tropopause. This
136 stable layer sloped upward with radius, which corresponded to an upward-sloping tropopause
137 radially outside of the eyewall region. Over the next 24 hours (Fig. 3d), as the storm's maximum
138 10-m wind speed remained quasi-steady near 80 m s^{-1} (Fig. 1), the tropopause-layer static stability
139 continued to increase. Within the eye, the layer between 16 and 19 km continued to destabilize,
140 and the cold-point tropopause height increased to a level above 21.5 km. This static stability
141 evolution closely follows that observed in Hurricane Patricia (2015; Duran and Molinari 2018).
142 Since most of the static stability variability

143 *b. Static stability budget analysis*

144 *(i) 0-24 hours* The first 24 hours of the simulation was characterized by a weakening of the
145 lower-stratospheric static stability maximum above 17 km (Fig. ??a, purple shading) and an in-
146 crease in static stability below (green shading). Although these tendencies extended out to the
147 200-km radius, they were particularly pronounced at innermost radii. A comparison of the contri-
148 butions of advection (Fig. ??b), vertical turbulence (Fig. ??c), and radiation (Fig. ??d) reveals that
149 advection is primarily responsible for the change in static stability during this period. ...Explain
150 this in the context of radial and vertical velocities...

151 *(ii) 24-48 hours* During the second day of the simulation, the lower-stratospheric stable layer
152 continued to weaken (Fig. 6a). This weakening trend in the 16.75-17.75-km layer extended from
153 the 50 km radius outward to past 200 km, and was primarily driven by advection (Fig. 6b). Below
154 this layer, static stability began to increase slightly. This stabilization had contributions from both

vertical turbulence (Fig. 6c) and radiation (Fig. 6d) in the 16-16.5-km layer. ...Explain this in context of mean vertical mixing coefficient and mean radiative heating tendency... Meanwhile, radially inward of 60 km, static stability below 17.5 km continued to weaken, primarily due to advective processes.

(iii) 48-72 hours The third day of the simulation marked a dramatic change in the structure of the tropopause-layer static stability tendencies. During this time, static stability increased markedly in an upward-sloping region within the 30-60-km radial band (Fig. 7a), and also increased within the 16.75-17.5-km layer out to at least the 200-km radius. As this layer stabilized, the layer immediately below it destabilized in a broad region extending from 60-200 km. Examination of the contribution from total advection (Fig. 7b) reveals that advection no longer dominates the static stability tendencies. Instead, a combination of vertical turbulence (Fig. 7c) and radiation (Fig. 7d) overcomes the destabilizing influence of advection to create the layer of increasing static stability. Meanwhile, the destabilizing influence of vertical turbulence in a broad region below 17 km combines with a small region of destabilization due to radiation in the 50-120-km radial band combine to destabilize the layer below 16.5 km in the 50-200-km radial band. Comparing the sum of advection and vertical turbulence (Fig. 7e) to the sum of advection, vertical turbulence, and radiation (Fig. 7f) reveals that radiation plays a fundamental role in the re-strengthening of the lower-stratospheric stable layer during this time.

(iv) 72-96 hours

5. Discussion

Radiative heating and turbulence viscosity figures?

176 Discuss how turbulence increases the static stability in some regions – vertical gradients of
177 turbulence intensity.

178 Dunion et al. speculate that the diurnal pulse only occurs in mature storms. Maybe the develop-
179 ment of the near-tropopause stable layer could partially explain the reason for this.

180 *Acknowledgments.* We are indebted to George Bryan for his continued development and support
181 of Cloud Model 1. We also thank Jeffrey Kepert, Robert Fovell, and Erika Navarro for helpful
182 conversations related to this work. ADD GRANT NUMBER

183 **References**

184 Bell, M. M., and Coauthors, 2016: Office of Naval Research Tropical Cyclone Intensity (TCI)
185 2015 NASA WB-57 High Density Dropsonde Sounding System (HDSS) data, version 1.0. doi:
186 10.5065/D6KW5D8M.

187 Bryan, G. H., 2012: Effects of surface exchange coefficients and turbulence length scales on the
188 intensity and structure of numerically simulated hurricanes. *Mon. Wea. Rev.*, **140**, 1125–1143.

189 Bryan, G. H., and R. Rotunno, 2009: The maximum intensity of tropical cyclones in axisymmetric
190 numerical model simulations. *Mon. Wea. Rev.*, **137**, 1770–1789.

191 Doyle, J. D., and Coauthors, 2017: A view of tropical cyclones from above: The Tropical Cyclone
192 Intensity (TCI) Experiment. *Bull. Amer. Meteor. Soc.*, **98**, 2113–2134.

193 Dunion, J. P., C. D. Thorncroft, and C. S. Velden, 2014: The tropical cyclone diurnal cycle of
194 mature hurricanes. *Mon. Wea. Rev.*, **142**, 3900–3919.

195 Duran, P., and J. Molinari, 2018: Dramatic inner-core tropopause variability during the rapid
196 intensification of Hurricane Patricia (2015). *Mon. Wea. Rev.*, **XXX**, XXX–XXX.

197 Iacono, M. J., J. S. Delamere, E. J. Mlawer, M. W. Shephard, S. A. Clough, and W. D. Collins,
 198 2008: Radiative forcing by long-lived greenhouse gases: Calculations with the AER radiative
 199 transfer models. *J. Geophys. Res.*, **113** (D13103).

200 Kimberlain, T. B., E. S. Blake, and J. P. Cangialosi, 2016: Tropical cyclone report: Hurricane
 201 Patricia. National Hurricane Center. [Available online at www.nhc.noaa.gov].

202 Markowski, P. M., and G. H. Bryan, 2016: LES of laminar flow in the PBL: A potential problem
 203 for convective storm simulations. *Mon. Wea. Rev.*, **144**, 1841–1850.

204 Rogers, R. F., S. Aberson, M. M. Bell, D. J. Cecil, J. D. Doyle, J. Morgerman, L. K. Shay, and
 205 C. Velden, 2017: Re-writing the tropical record books: The extraordinary intensification of
 206 Hurricane Patricia (2015). *Bull. Amer. Meteor. Soc.*, **98**, 2091–2112.

207 Rotunno, R., and K. A. Emanuel, 1987: An air-sea interaction theory for tropical cyclones. Part II:
 208 Evolutionary study using a nonhydrostatic axisymmetric numerical model. *J. Atmos. Sci.*, **44**,
 209 542–561.

210 Thompson, G., R. M. Rasmussen, and K. Manning, 2004: Explicit forecasts of winter precipitation
 211 using an improved bulk microphysics scheme. Part I: Description and sensitivity analysis. *Mon.*
 212 *Wea. Rev.*, **132**, 519–542.

213 LIST OF FIGURES

214	Fig. 1.	The maximum 10-m wind speed (top panel; m s^{-1}) and minimum sea-level pressure (bottom	
215		panel; hPa) in the simulated storm (blue lines) and from Hurricane Patricia's best track (red	
216		stars).	15
217	Fig. 2.	Left panels: Twenty-four-hour changes in squared Brunt-Väisälä frequency ($N^2 \cdot 10^{-4} \text{ s}^{-2}$)	
218		over (a) 0-24 hours, (b) 24-48 hours, (c) 48-72 hours, (d) 72-96 hours. Middle Panels: The	
219		N^2 change over the same time periods computed using Eq. 6. Right Panels: The budget	
220		residual over the same time periods, computed by subtracting the budget change (middle	
221		column) from the model change (left column).	16
222	Fig. 3.	Twenty-four-hour averages of squared Brunt-Väisälä frequency (10^{-4} s^{-2}) over the first four	
223		days of the simulation. Orange lines represent the cold-point tropopause determined by the	
224		mean temperature field over the same time periods.	17
225	Fig. 4.	Time series of the contribution of each of the budget terms to the time tendency of the	
226		squared Brunt-Väisälä frequency (N^2 ; 10^{-4} s^{-2}). For each budget term, the absolute value	
227		of the N^2 tendency is averaged temporally over 1-hour periods (using output every minute),	
228		and spatially in a region extending from 0 to 200 km radius and 14 to 21 km altitude.	18
229	Fig. 5.	(a) Total change in N^2 over the 0-24-hour period ($10^{-4} \text{ s}^{-2} (24 \text{ hr})^{-1}$) and the contributions to	
230		that change from (b) the sum of horizontal and vertical advection, (c) vertical turbulence, (d)	
231		longwave and shortwave radiation, (e) the sum of horizontal advection, vertical advection,	
232		and vertical turbulence, and (f) the sum of horizontal advection, vertical advection, vertical	
233		turbulence, and longwave and shortwave radiation.	19

234	Fig. 6.	As in Fig. 5, but for the 24-48-hour period.	20
235	Fig. 7.	As in Fig. 5, but for the 48-72-hour period.	21
236	Fig. 8.	Radial velocity (m s^{-1} ; filled contours), potential temperature (K; thick black contours), and	
237		cold point tropopause height (orange lines) averaged over (a) 0-24 hours, (b) 24-48 hours,	
238		and (c) 48-72 hours.	22
239	Fig. 9.	Vertical velocity (cm s^{-1} ; filled contours), potential temperature (K; thick black contours),	
240		and cold point tropopause height (orange lines) averaged over (a) 0-24 hours, (b) 24-48	
241		hours, and (c) 48-72 hours.	23
242	Fig. 10.	Total condensate mixing ratio (g kg^{-1}) and cold point tropopause height (orange lines) aver-	
243		aged over (a) 0-24 hours, (b) 24-48 hours, and (c) 48-72 hours.	24
244	Fig. 11.	Radiative heating rate (K hr^{-1}) and cold point tropopause height (orange lines) averaged over	
245		(a) 0-24 hours, (b) 24-48 hours, and (c) 48-72 hours.	25
246	Fig. 12.	Vertical eddy diffusivity ($\text{m}^2 \text{s}^{-2}$; filled contours), cold point tropopause height (cyan lines),	
247		and radial velocity (m s^{-1} ; thick black lines) averaged over (a) 0-24 hours, (b) 24-48 hours,	
248		and (c) 48-72 hours.	26

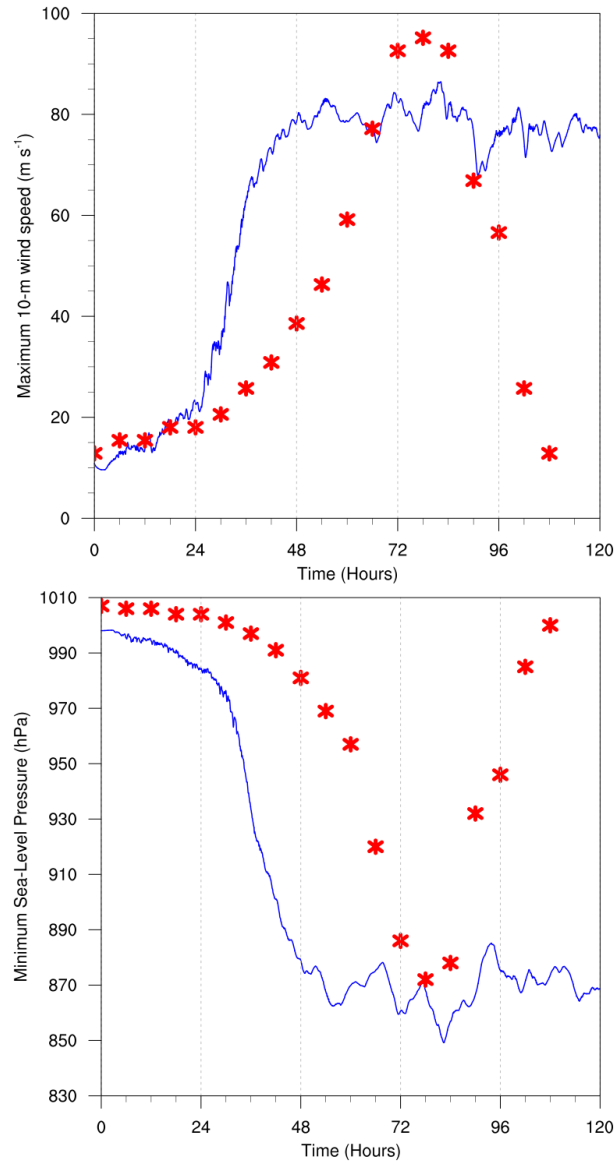


FIG. 1. The maximum 10-m wind speed (top panel; m s^{-1}) and minimum sea-level pressure (bottom panel; hPa) in the simulated storm (blue lines) and from Hurricane Patricia's best track (red stars).

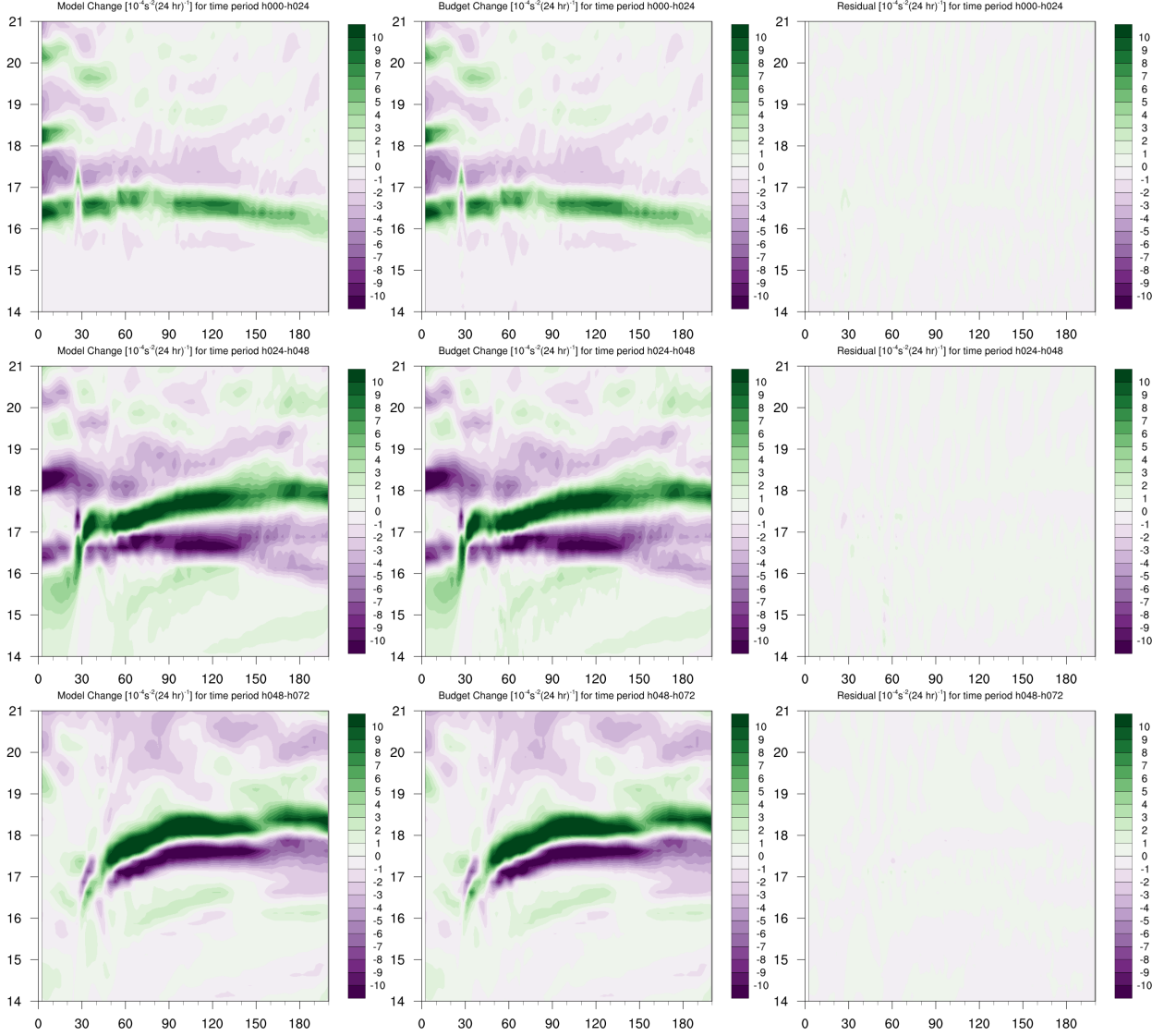


FIG. 2. Left panels: Twenty-four-hour changes in squared Brunt-Väisälä frequency (N^2 10^{-4} s^{-2}) over (a) 0-24 hours, (b) 24-48 hours, (c) 48-72 hours, (d) 72-96 hours. Middle Panels: The N^2 change over the same time periods computed using Eq. 6. Right Panels: The budget residual over the same time periods, computed by subtracting the budget change (middle column) from the model change (left column).

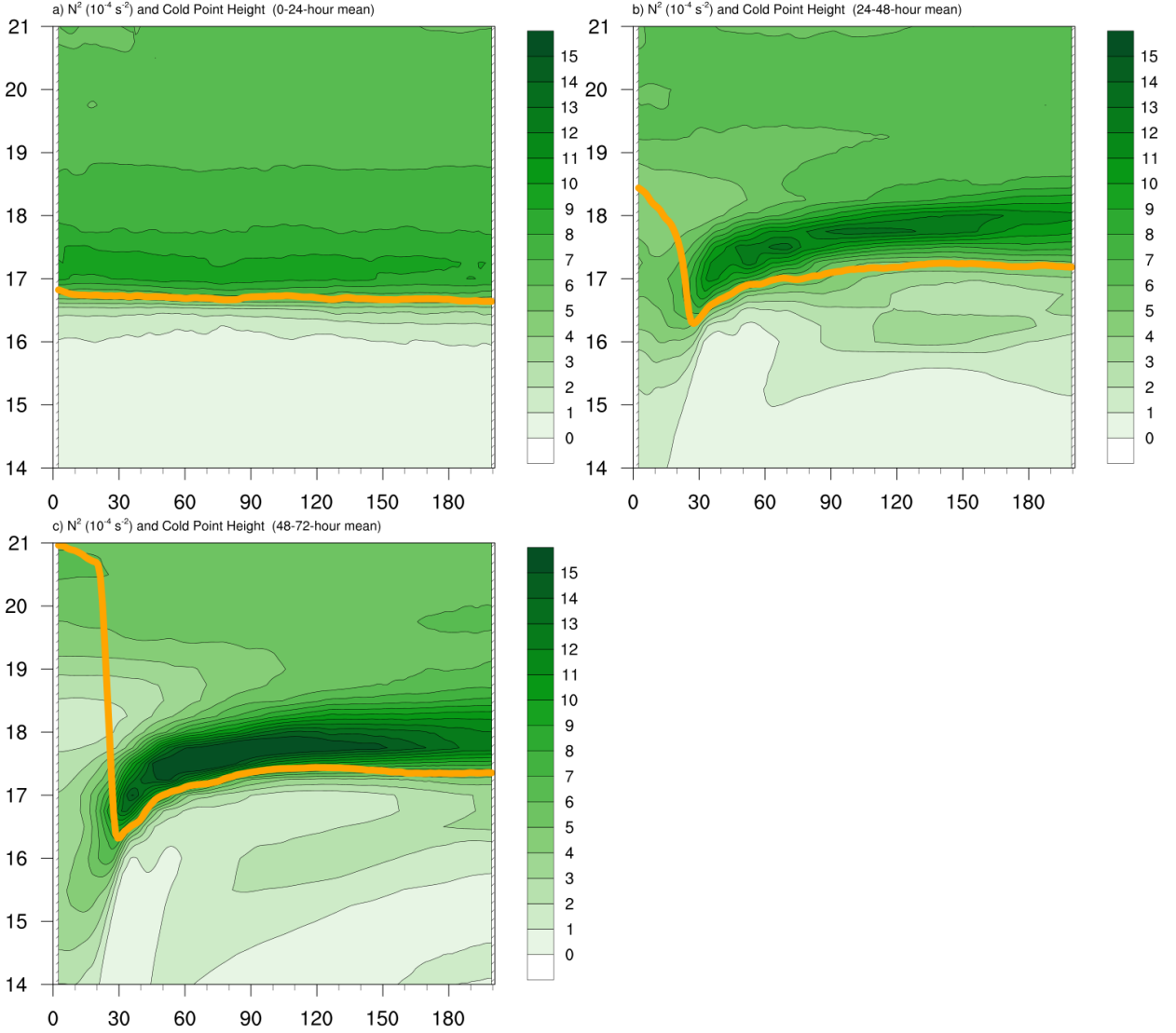
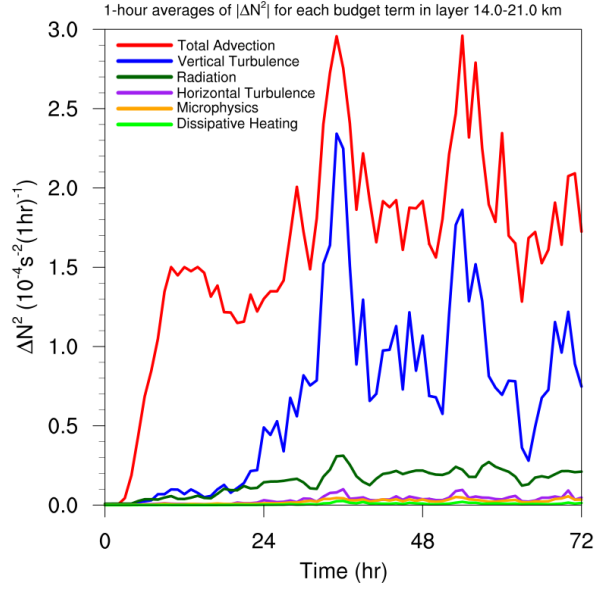


FIG. 3. Twenty-four-hour averages of squared Brunt-Väisälä frequency (10^{-4} s^{-2}) over the first four days of the simulation. Orange lines represent the cold-point tropopause determined by the mean temperature field over the same time periods.



258 FIG. 4. Time series of the contribution of each of the budget terms to the time tendency of the squared
 259 Brunt-Väisälä frequency (N^2 ; 10^{-4} s^{-2}). For each budget term, the absolute value of the N^2 tendency is averaged
 260 temporally over 1-hour periods (using output every minute), and spatially in a region extending from 0 to 200
 261 km radius and 14 to 21 km altitude.

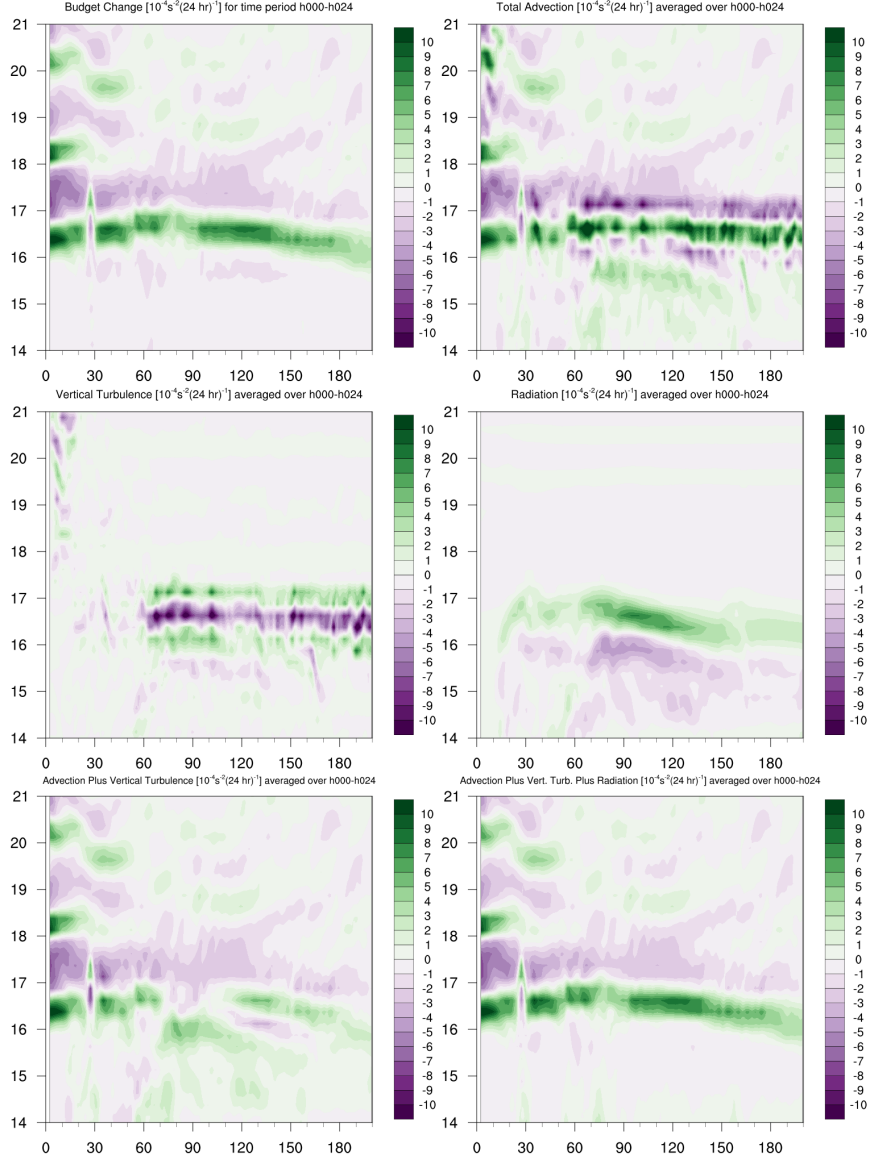


FIG. 5. (a) Total change in N^2 over the 0-24-hour period ($10^{-4} \text{ s}^{-2} (24 \text{ hr})^{-1}$) and the contributions to that change from (b) the sum of horizontal and vertical advection, (c) vertical turbulence, (d) longwave and shortwave radiation, (e) the sum of horizontal advection, vertical advection, and vertical turbulence, and (f) the sum of horizontal advection, vertical advection, vertical turbulence, and longwave and shortwave radiation.

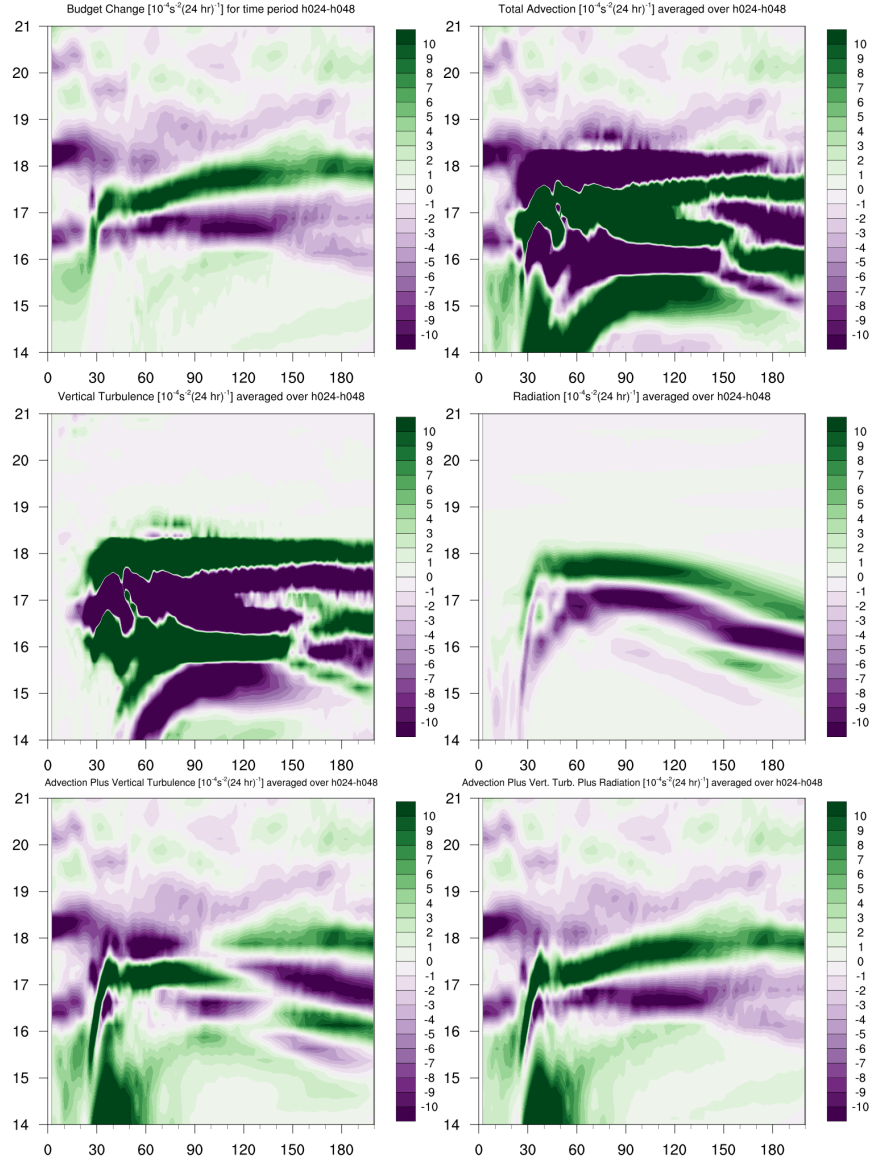


FIG. 6. As in Fig. 5, but for the 24-48-hour period.

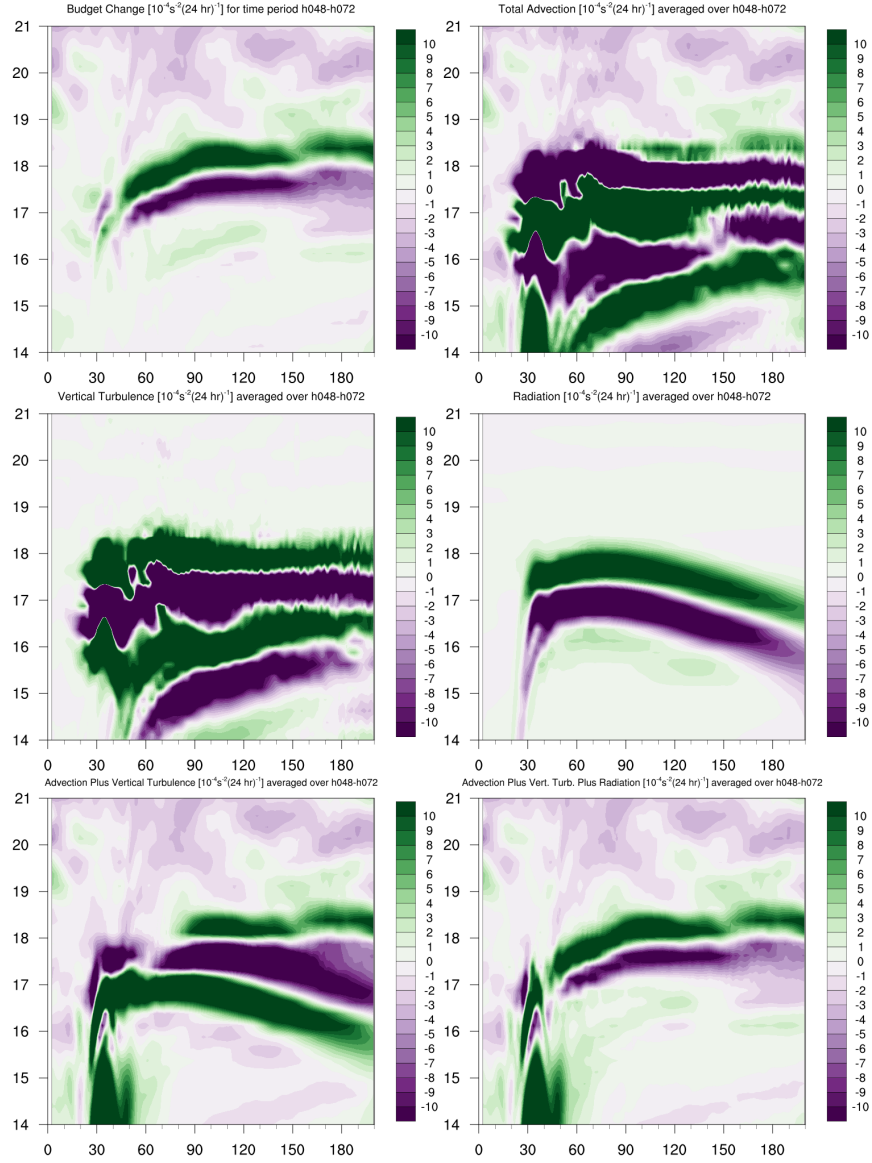


FIG. 7. As in Fig. 5, but for the 48-72-hour period.

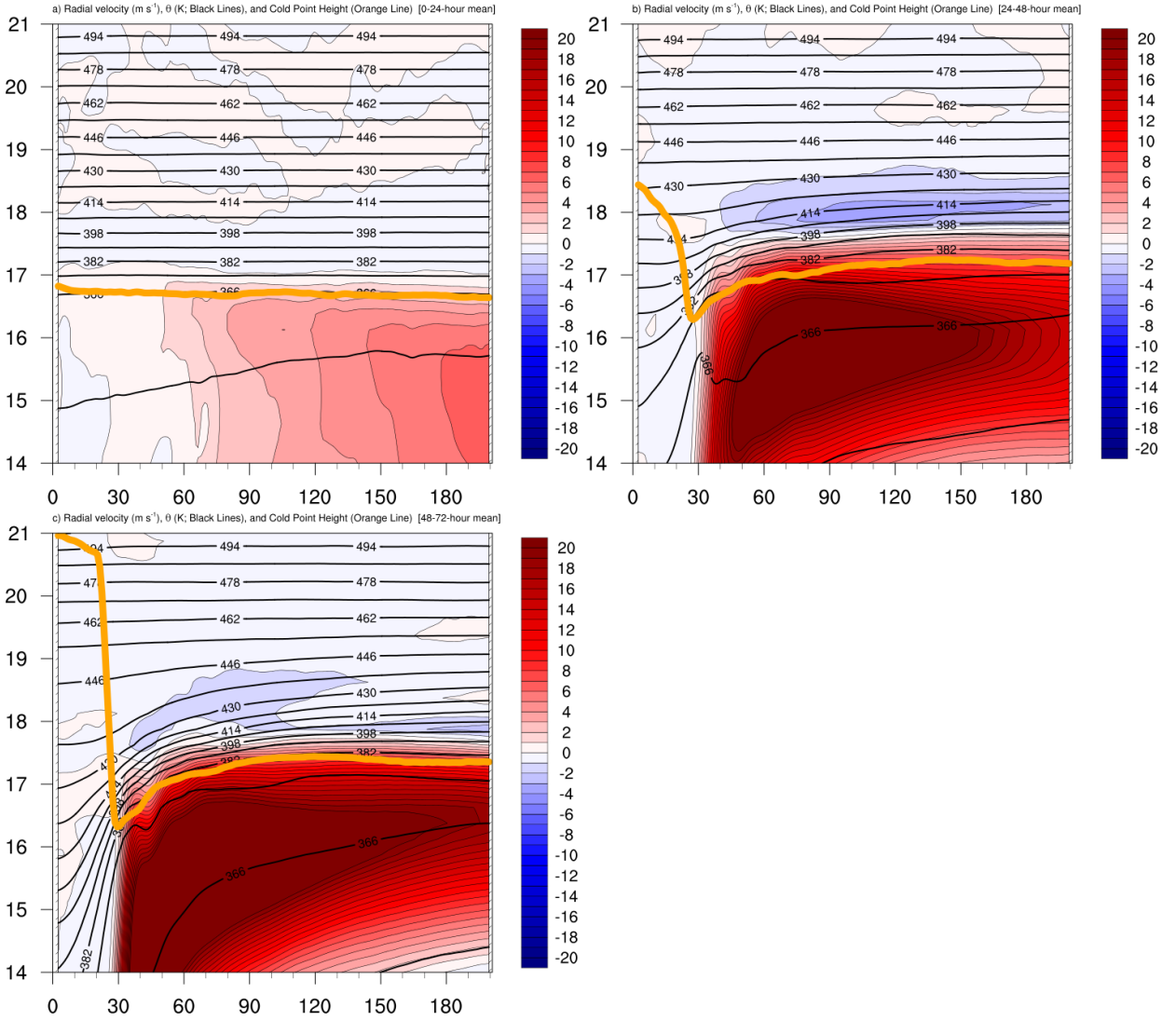


FIG. 8. Radial velocity (m s^{-1} ; filled contours), potential temperature (K; thick black contours), and cold point tropopause height (orange lines) averaged over (a) 0-24 hours, (b) 24-48 hours, and (c) 48-72 hours.

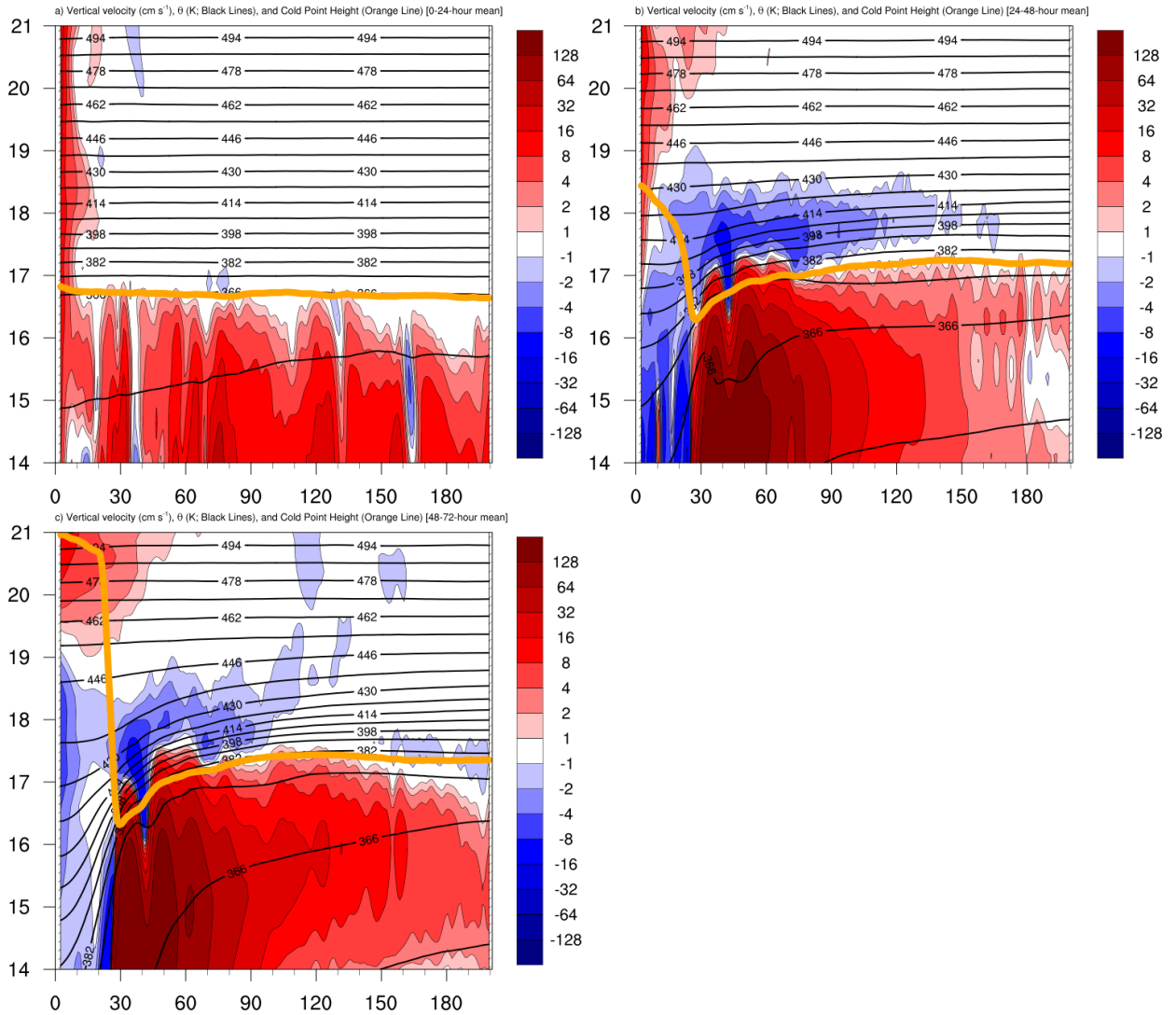


FIG. 9. Vertical velocity (cm s^{-1} ; filled contours), potential temperature (K; thick black contours), and cold point tropopause height (orange lines) averaged over (a) 0-24 hours, (b) 24-48 hours, and (c) 48-72 hours.

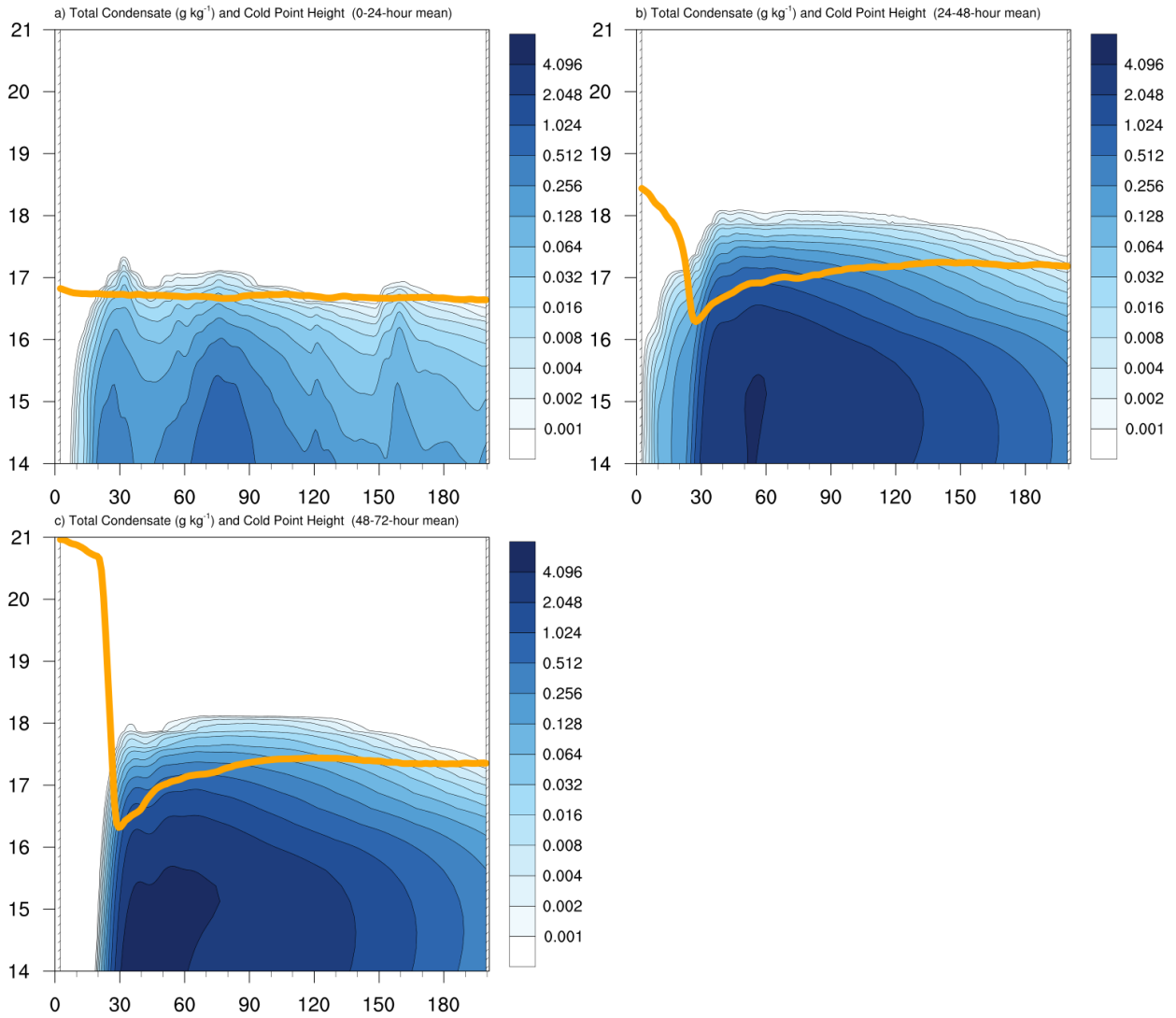


FIG. 10. Total condensate mixing ratio (g kg^{-1}) and cold point tropopause height (orange lines) averaged over (a) 0-24 hours, (b) 24-48 hours, and (c) 48-72 hours.

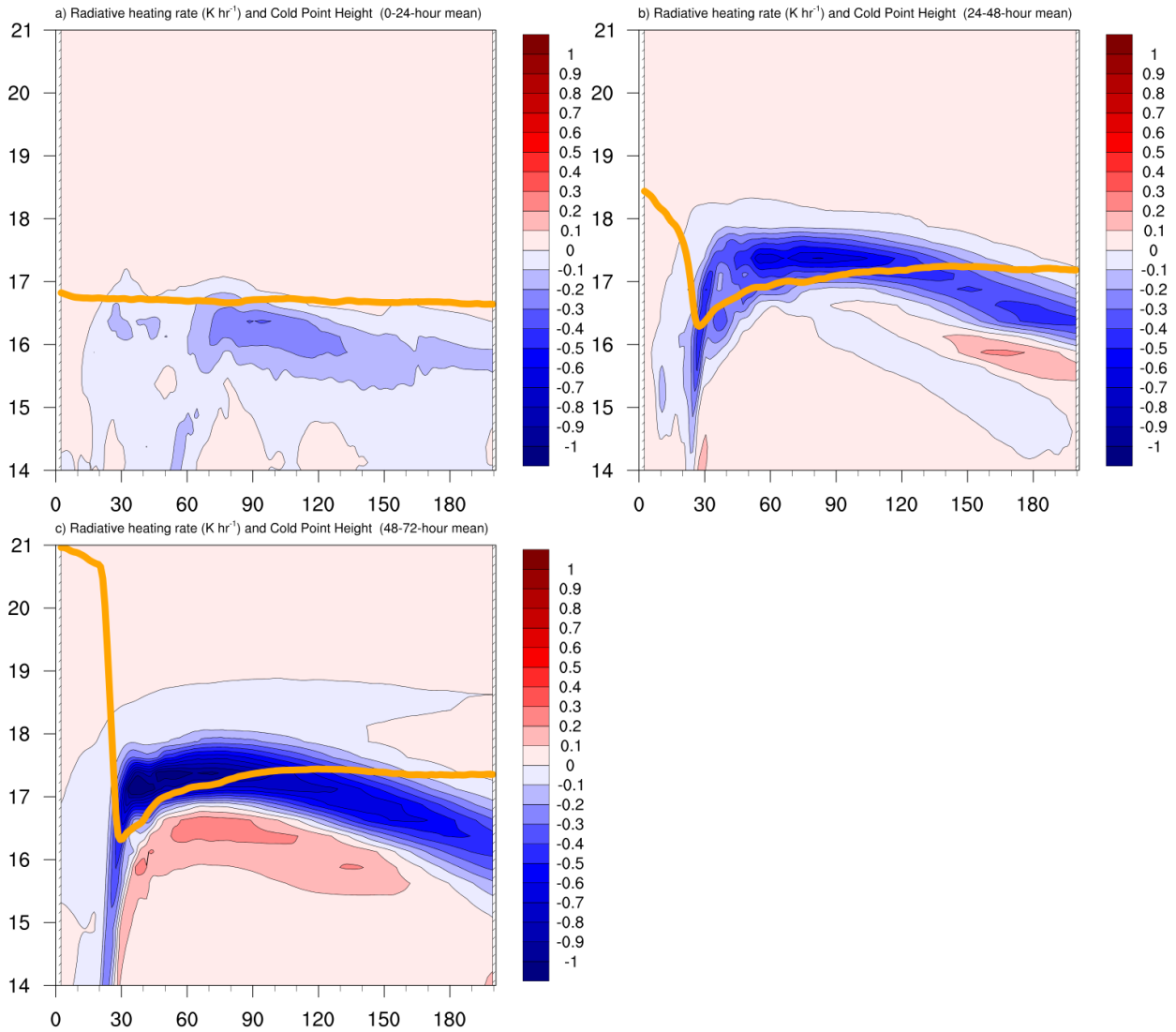


FIG. 11. Radiative heating rate (K hr^{-1}) and cold point tropopause height (orange lines) averaged over (a) 0-24 hours, (b) 24-48 hours, and (c) 48-72 hours.

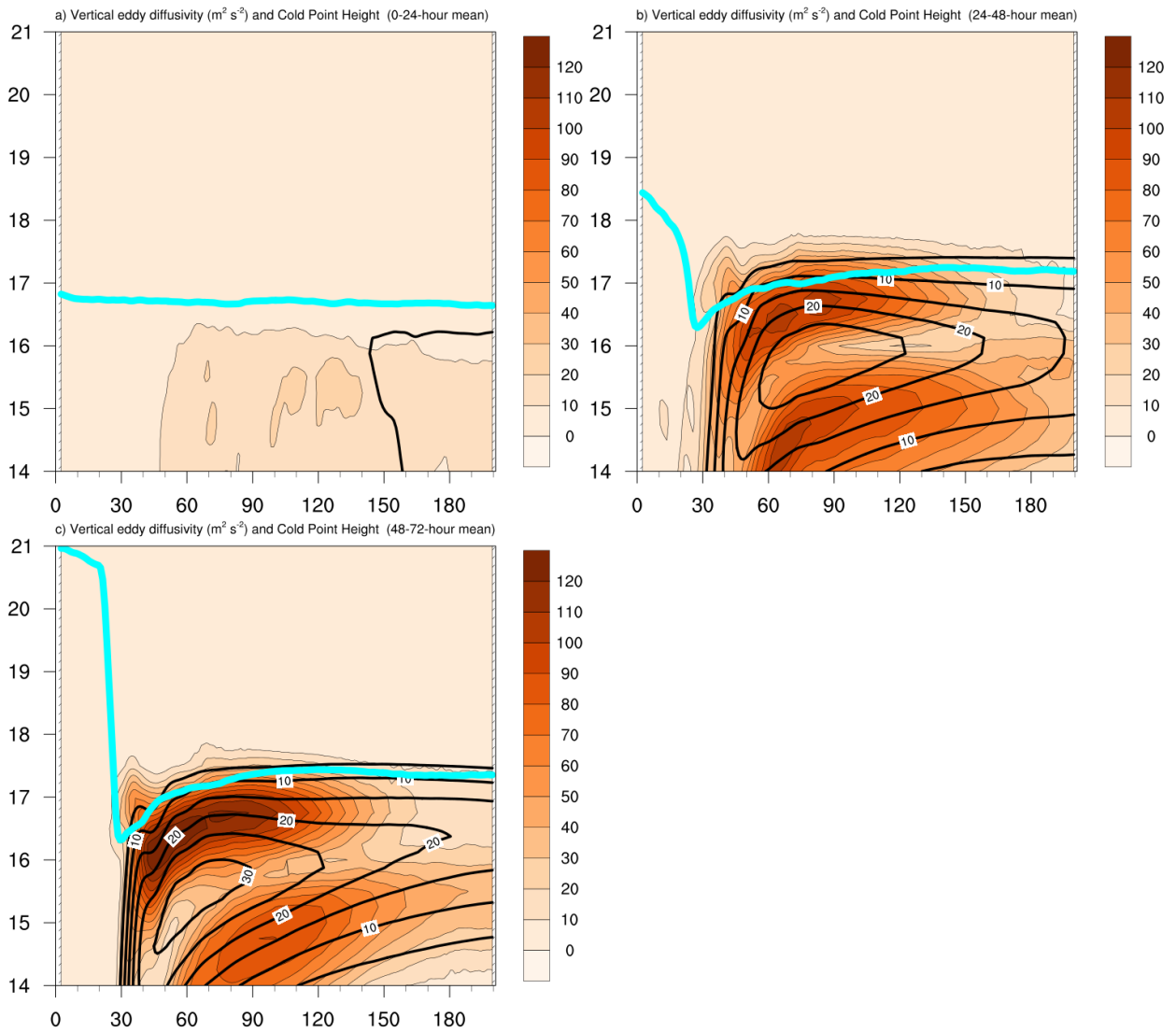


FIG. 12. Vertical eddy diffusivity ($\text{m}^2 \text{s}^{-2}$; filled contours), cold point tropopause height (cyan lines), and radial velocity (m s^{-1} ; thick black lines) averaged over (a) 0-24 hours, (b) 24-48 hours, and (c) 48-72 hours.